

Landing-Induced Viscoelastic Changes in an Anthropomorphic Foot Joint Structure are Modulated by Foot Structure and Posture

Satoru Hashimoto¹, Yinlai Jiang², Hiroshi Yokoi^{1,2}, and Shunta Togo^{1,2*}

¹Department of Mechanical and Intelligent System Engineering, Graduate School of Informatics and Engineering, The University of Electro-Communications, Tokyo, Japan.

²Center for Neuroscience and Biomedical Engineering, The University of Electro-Communications, Tokyo, Japan.

*Address correspondence to: s.togo@uec.ac.jp

Abstract

Cadaveric studies have provided important insights into the mechanics of the human foot arch and plantar fascia. However, repeatedly probing posture-dependent viscoelastic responses immediately after landing impact is difficult in biological specimens, leaving the contribution of skeletal architecture to landing dynamics incompletely understood. In this study, we developed an anthropomorphic foot joint structure aimed at replicating the skeletal geometry of the human foot. Using a vertical drop apparatus that simulates landing and a viscoelastic system-identification model, we investigated how skeletal structure and posture modulate the apparent post-impact viscoelastic response. The results show that the multi-jointed anthropomorphic structure exhibited a higher damping ratio than simplified flat and rigid feet. Moreover, ankle dorsiflexion and toe extension systematically shifted the identified parameters, reducing the damping ratio under the tested conditions. Taken together, these findings indicate that an arch-like, multi-jointed skeletal architecture can enhance impact attenuation in an anthropomorphic mechanical foot, and that morphology and passive posture alone can tune the trade-off between attenuation and rebound. The observed posture-dependent trends are qualitatively consistent with reported differences in human landing strategies, suggesting that skeletal architecture may partly account for the modulation. Furthermore, these results highlight the engineering advantage of anatomically informed skeletal replication for achieving human-like apparent viscoelastic behavior through postural adjustment during landing.

INTRODUCTION

Humans acquired bipedal locomotion through a long evolutionary process. During this process, the foot evolved from a structure with opposing grasping functions, as seen in apes, to an arched structure [1–3]. It is believed that this structural change in the foot occurred as the living environment of human ancestors changed from trees to the ground [4]. When comparing the morphology of the feet of humans and apes, it can be observed that humans have short toes aligned in the same direction, and their metatarsals and tarsals are thick and large [1–3]. In addition, they have a well-developed band of elastic tissue called the plantar fascia, which supports the arch of the foot and adaptively changes the rigidity of the foot [5]. The human foot is thought to have acquired functions such as shock absorption during landing, adaptation to uneven surfaces, and contribution to propulsion during walking [6–9].

The locomotion styles of terrestrial mammals can be categorized into three types—unguligrade, digitigrade, and plantigrade—based on the morphological characteristics and posture of the foot [10, 11]. The unguligrade style, observed in animals such as horses and cattle, involves propulsion using hooves. The digitigrade style, seen in animals such as dogs,

cats, and birds, involves walking with the heel elevated and making contact with the ground only through the toes. The plantigrade style, found in animals, such as bears and rodents, involves placing the entire sole of their foot, including the heel, on the ground. Humans are classified as plantigrades; however, unlike other plantigrades, humans exhibit distinct postural transitions while walking, landing on the heel, and propelling with the toes. Furthermore, during running, humans transition to a digitigrade-like locomotion, landing on the extended toes [12]. Such variations in morphology and posture are expected to alter the balance between energy dissipation and elastic energy storage at foot-ground contact, thereby modulating impact attenuation and rebound. A compact way to quantify this balance is through apparent viscoelastic properties (effective stiffness and damping) identified from the transient force response during landing. Therefore, although various properties of terrestrial mammalian feet have been discussed (e.g., moment arms and resistance to load stress) [11, 13], this study specifically focuses on landing-induced viscoelastic responses.

Several simulation analyses using mathematical models have been conducted to investigate the viscoelastic properties of the human foot [14–16]. However, the viscoelastic properties identified from such models include contributions from elements such as the soft tissues of the foot (e.g., skin and subcutaneous tissues) and footwear. As a result, the viscoelastic properties inherent to the musculoskeletal system itself have not been addressed directly. Furthermore, in some studies, the viscoelastic coefficients of the foot have been determined in relation to posture using mathematical modeling approaches. The findings revealed that the viscous coefficient peaks during foot-ground contact, while the elastic coefficient peaks during toe-off in walking [17, 18]. However, the influence of soft tissues has not been excluded in these studies, leaving it unclear whether the foot exhibits viscoelastic changes derived solely from the musculoskeletal system. Additionally, because these findings are based on simulations, it is necessary to experimentally investigate the viscoelastic changes in the musculoskeletal system of the foot in the real world.

One method to systematically and experimentally investigate the functions and properties of individual components of the human foot involves using cadaveric feet. Wright et al. extracted specimens of the plantar fascia from cadaveric feet and examined their elastic properties [19]. Similarly, Carlson et al. investigated the relationship between the Achilles tendon tension and plantar fascia strain and revealed that toe extension contributes to the tightening of the plantar fascia [20]. The use of cadaveric feet enables researchers to obtain data on specific tissues or structures that are otherwise difficult to measure *in vivo*. However, this approach has several limitations. Ethical considerations pose significant challenges and the limited availability of samples makes it difficult to collect data from young or healthy individuals. Furthermore, concerns also exist regarding alterations in the properties of biological tissues owing to postmortem changes or freezing processes. To investigate viscoelastic changes during landing, as highlighted in this study, it is necessary to repeatedly strike the foot against the ground while varying the posture. Such experimental requirements render the use of cadaveric feet unsuitable.

As an alternative to using cadaveric feet, a robotics-based approach can be considered, in which foot mechanics that mimic the structure of the human foot are developed and used for experimentation. This approach enables researchers to adjust various parameters, such as the skeletal structure and mechanical properties of biological tissues, enabling easier analysis of human foot dynamics than using cadaveric feet. Humanoid robotics offer relevant insights from the perspective of engineered feet. Many humanoid robots, such as Honda's ASIMO [21] and Boston Dynamics ATLAS [22], feature flat-sole foot designs

owing to their advantages in terms of control and design simplicity. However, recent efforts have been inspired by human-arch structures to design linkage-based systems [23, 24]. Furthermore, attempts have been made to design mechanisms inspired by the skeletal structure and plantar fascia of the human foot [25, 26]. Despite these advances, to the best of our knowledge, no prior work has both precisely reproduced the shape of human bones or directly mimics the musculoskeletal structure; moreover, the viscoelastic behavior of anthropomimetic foot mechanisms during landing has not yet been reported. Notably, in the field of robotic hands and arms, several examples of designs mimicking human bones and ligament structures have been reported, and developments toward flexible and dexterous hand mechanisms similar to those of humans are underway [27–33].

In this study, we hypothesize that, in an anatomically grounded anthropomimetic skeletal–ligamentous architecture, landing posture can modulate the apparent viscoelastic response observed immediately after impact. This study has two objectives: (i) to develop an anthropomimetic foot joint structure aimed at replicating key human skeletal geometry and ligamentous constraints, rather than a generic robotic foot; and (ii) to test this hypothesis experimentally using the developed anthropomimetic foot joint structure as a physical model under controlled landing impacts. The methodology entails the following steps. First, inspired by the techniques used in biomimetic robotic hands [27, 31], we fabricated an anthropomimetic foot joint structure using 3D-printed plastic parts and flexible materials. Second, we conducted impact loading experiments by dropping the foot structures while varying their structures, i.e., the shape and degrees of freedom (DoF), and postures, that is, the ankle angle and toe angle. Finally, we analyzed the changes in the viscoelastic properties under different landing conditions by examining the measured impact forces transmitted to the ankle and identifying the viscoelastic coefficients using a simple spring-mass-damper model.

MATERIALS AND METHODS

Experimental design

We developed an anthropomimetic foot joint structure and two simplified counterparts (rigid and flat) with matched overall dimensions and mass, enabling systematic comparisons of skeletal structure and landing posture (Figs. 1 and 2). We then conducted controlled free-fall impact loading experiments to quantify how foot skeletal structure and landing posture modulate the immediate post-landing viscoelastic response. The study comprised three predefined comparisons (Fig. 3): (1) skeletal structure (flat, rigid, and soft/anthropomimetic), (2) ankle angle θ_a (-30° , -15° , 0° , and 15°), and (3) toe angle θ_t (0° , 15° , 30° , and 45°) adjusted via the toe-extension tendon. For each condition, the foot was dropped from four initial heights (50, 100, 150, and 200 mm) with 10 repeated trials. Impact force transmitted to the ankle (load cell), foot height change (infrared distance sensor), and landing motion (video) were recorded. We quantified peak force and identified viscoelastic parameters and damping ratio from the impact-force waveform. Details of the foot structures, experimental apparatus, and analysis pipeline are described below.

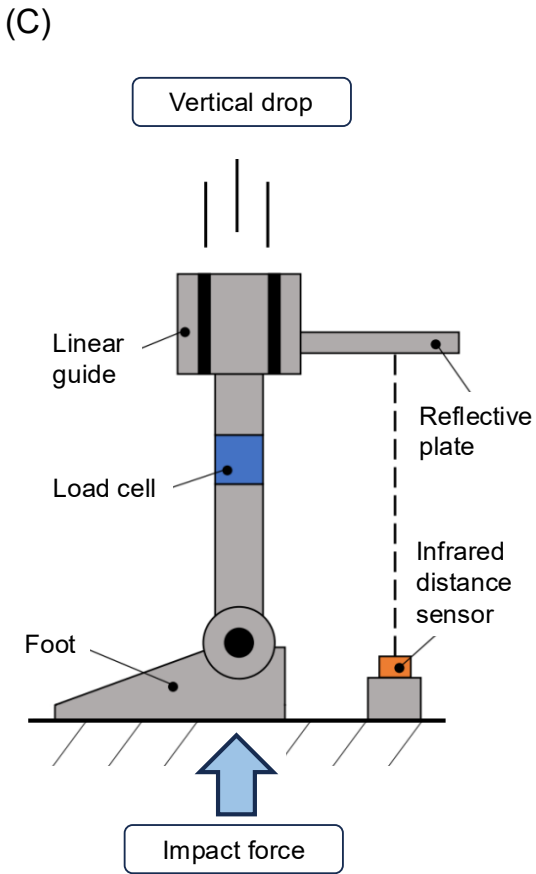
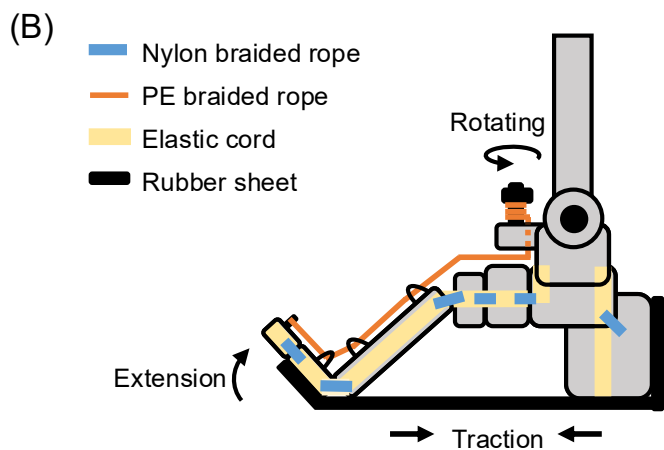
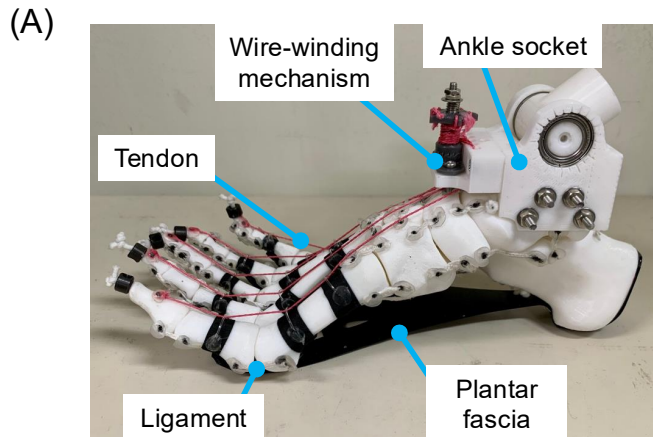


Fig. 1. Overview of the anthropomimetic foot joint structure and experimental apparatus. (A) Photograph of the fabricated anthropomimetic foot joint structure. (B) Schematic of the anthropomimetic foot joint structure. Nylon braided ropes are attached at positions corresponding to human ligaments to restrict the range of motion. Joint restorative force is incorporated into each joint by threading elastic cords through the hollow, 3D-printed skeletal parts. Polyethylene (PE) braided ropes are used as tendons, enabling toe extension and tensioning of the plantar fascia, represented by a rubber sheet, through a winding mechanism attached to the ankle. (C) Schematic of the experimental apparatus. The fabricated foot joint structure is allowed to free-fall along a linear guide. The impact force transmitted to the ankle is measured using a load cell attached to the ankle, and the position of the foot joint structure is recorded using infrared distance sensors integrated into the experimental apparatus.

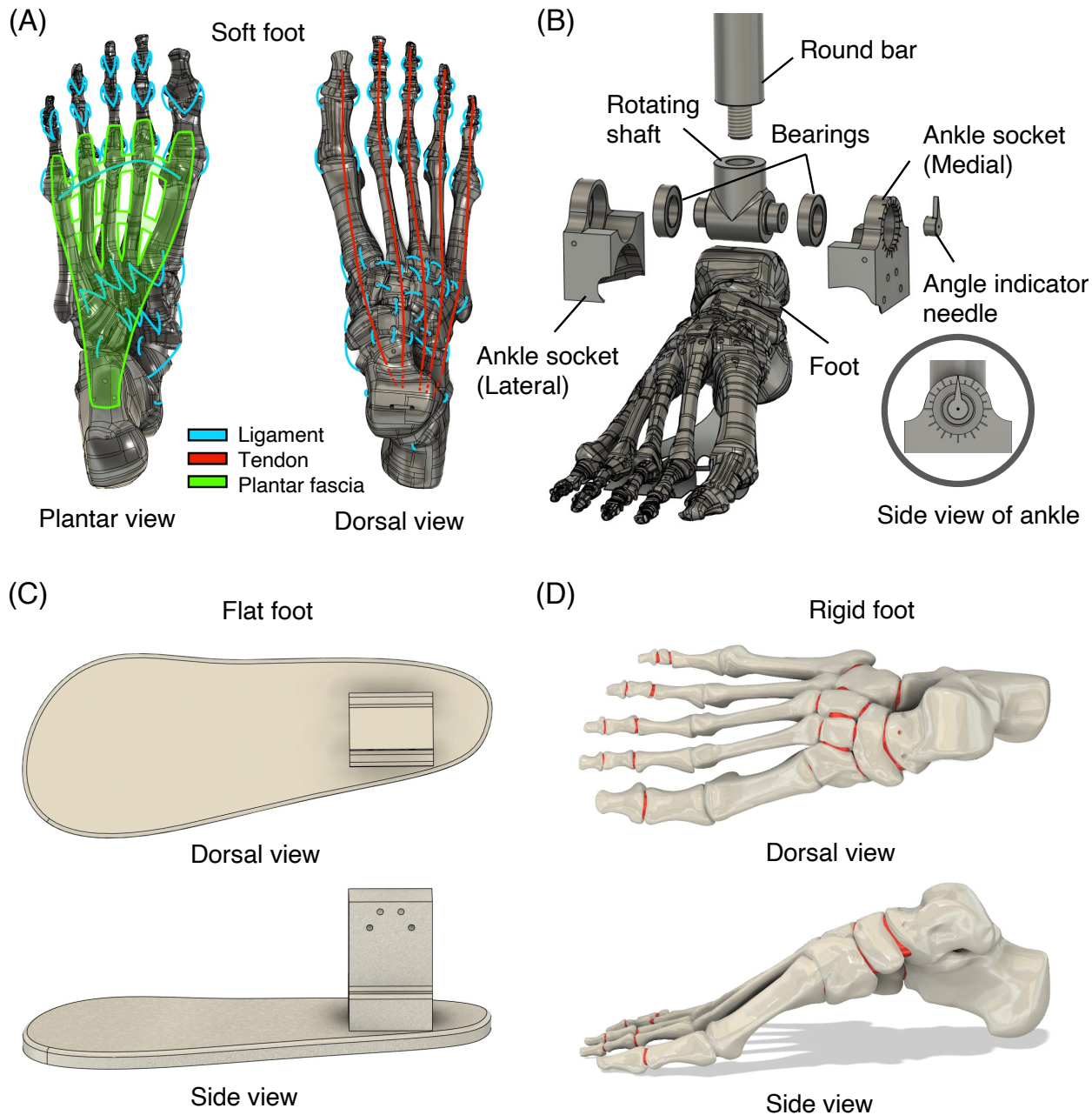


Fig. 2. Design of each foot structure used in the experiments. (A) Design and attachment positions of the ligaments, tendons, and plantar fascia in the anthropomimetic foot joint structure (Soft foot). The attachment positions and shapes of each biological structure are designed based on anatomical illustrations from anatomical references. (B) Design of the ankle socket for adjusting ankle angles. The ankle socket is fixed to the talus using screws and nuts, with a shaft rotating via bearings. The diagram enclosed at the bottom right circle provides a side view of the angle indicator needle used to confirm the ankle angle. (C) 3D CAD model of the flat foot and (D) 3D CAD model of the rigid foot designed for comparative experiments. The red-highlighted areas indicate the regions where the small joints (except for the MTP joint) are rigidly connected.

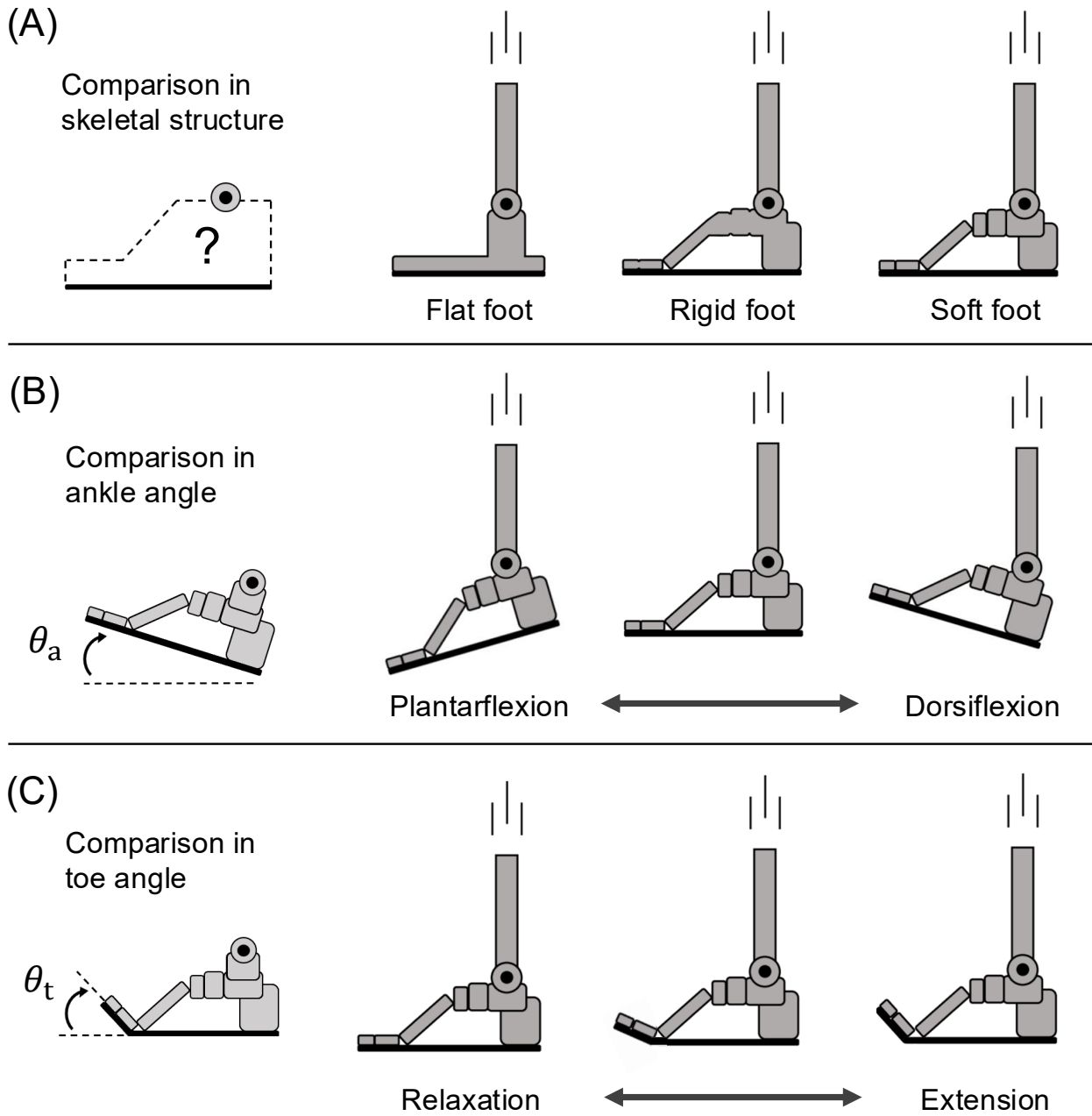


Fig. 3. Three comparative conditions in the impact loading experiments. (A) Differences in the skeletal structure. The landings of three types of foot structures—flat foot, rigid foot, and soft foot (anthropomimetic foot joint structure)—are compared. (B) Differences in the ankle angle. Landings with varying ankle angles θ_a are compared. The ankle angle θ_a is defined as zero degrees when the sole is horizontal, with dorsiflexion considered in the positive direction. (C) Differences in toe angle. Landings with varying toe angles θ_t are compared. The toe angle θ_t is defined as zero degrees when the toes are relaxed, with extension considered in the positive direction.

Development of the anthropomimetic foot joint structure

An anthropomimetic foot joint structure (human right foot) designed to approximate key skeletal geometry and ligamentous constraints was developed (Fig. 1). Figure 2 shows a 3D CAD model (Autodesk Fusion, Autodesk Inc., USA) of the foot and the attachment positions of the ligaments, tendons, and plantar fascia. The 3D CAD data for the developed foot structures (anthropomimetic, rigid, and flat) and the custom 3D-printed parts used in the experimental apparatus are publicly available in a GitHub repository

(<https://github.com/TogoLab/anthropomimetic-foot-joint-structure>) to facilitate reproducibility. The shapes and attachment positions of each structure were designed based on anatomical references [34].

The skeletal parts of the anthropomimetic foot joint structure were created using 3D scan data obtained from the BodyParts3D web resource provided by the Life Science Integrated Database Center (DBCLS) [35]. The data were edited using the 3D CAD software and 3D printed with a poly-lactic acid (PLA) filament (Raise3D Pro3, Raise 3D Technologies, Inc., USA). The ligaments that restricted the range of motion of the joints were recreated using braided nylon ropes with a diameter of 1.15 mm, fixed to the joint areas. The ends of the braided ropes were hardened using a glue gun, perforated, and secured using M1 screws. The plantar fascia, which supports the arch structure, was created by cutting a rubber sheet approximately 3 mm thick. The sheet was then screwed onto the calcaneus and proximal phalanges of the toes. To standardize the material of the foot sole during the drop experiments, regardless of the landing posture, the same rubber sheet was attached to the calcaneus. PE-braided ropes with a diameter of 0.52 mm were employed to enable the tendons to extend the toes. These ropes were wound using a mechanism that involved combining a clutch and spring mounted on the ankle (Fig. 1B). The winding mechanism was fabricated using a stereolithography 3D printer (Form3, Formlabs Inc., USA) with Tough 2000 resin. In human joints, the joint capsule provides a restoring force and maintains the relative positions of bones. The function was replicated in the anthropomimetic foot joint structure by hollowing out the bones and threading elastic cords (diameter of 2 mm) through their interiors.

To adjust the ankle angle of the foot, an ankle socket, as shown in Fig. 2B, was 3D printed using PLA filament. The interior of the socket was designed to fit the shape of the talus and secured to the talus using four screws and M3 nuts. In addition, the rotational axis of the ankle, with an attached round rod, was fixed to the ankle socket through the bearings. An angle indicator needle mounted on the rotational axis, combined with grooves marked at 15° intervals on the ankle socket, allowed precise measurement of the ankle angle (Fig. 2B). The clutch mechanism for winding the toe extension tendon rope was mounted on the ankle socket. The fabricated anthropomimetic foot joint structure had the following dimensions: foot length 218 mm, foot width 82 mm, height (from the sole to the rotational center of the ankle) 88 mm, and weight 136 g.

In addition to the anthropomimetic foot joint structure (soft foot), the flat foot and rigid foot were also fabricated for comparative experiments. The 3D CAD models are shown in Figs. 2C and 2D. A flat foot is a rigid structure with zero DoFs, commonly used in humanoid robots, and features a flat sole. Its external shape was designed based on the 3D bone data used for the anthropomimetic foot joint structure, ensuring that the sole closely follows the contour of sole of the anthropomimetic foot. To isolate the effects of the skeletal structural differences in the drop experiments, the same rubber sheet used for the plantar fascia of the anthropomimetic foot joint structure was attached to the sole of a flat foot. The rigid foot was designed by rigidly connecting all the small joints of the anthropomimetic foot joint structure, except for the MTP joint, which resulted in a structure in which only the toes retained mobility (five-DoFs). The ligaments of the MTP joint and the internal elastic cord structure for the restoring force were designed in the same manner as the anthropomimetic foot joint structure. In addition, the same rubber sheet used for the plantar fascia was attached to the sole, and an identical rubber sheet was affixed to the calcaneus. These foot structures were designed such that, when fitted with the ankle socket, the height from the

sole to the rotational axis would be identical to that of the anthropomimetic foot joint structure at 88 mm. Furthermore, to ensure that the total weight matched the anthropomimetic foot weight of 136 g, oil clay was added near the ankle for weight adjustment. This ensured that the potential energy at a given drop height remained constant across the flat foot, rigid foot, and soft foot.

Experimental apparatus

An experimental apparatus was constructed to measure the impact force transmitted to the ankle and foot position upon landing after a free fall. Fig. 4A presents an overview of the experimental apparatus. The main structure of the apparatus was built using 30 mm × 30 mm aluminum frames, and a linear guide and rails were used to implement the vertical drop mechanism for the foot structures. The effects of friction and variations in the drop angle were minimized by allowing the foot structures to slide between the two linear rails, improving the reproducibility of the experiment. To record the behavior of the foot structures during the drop, a camera (iPhone XR, Apple, USA) was fixed in front of the experimental setup.

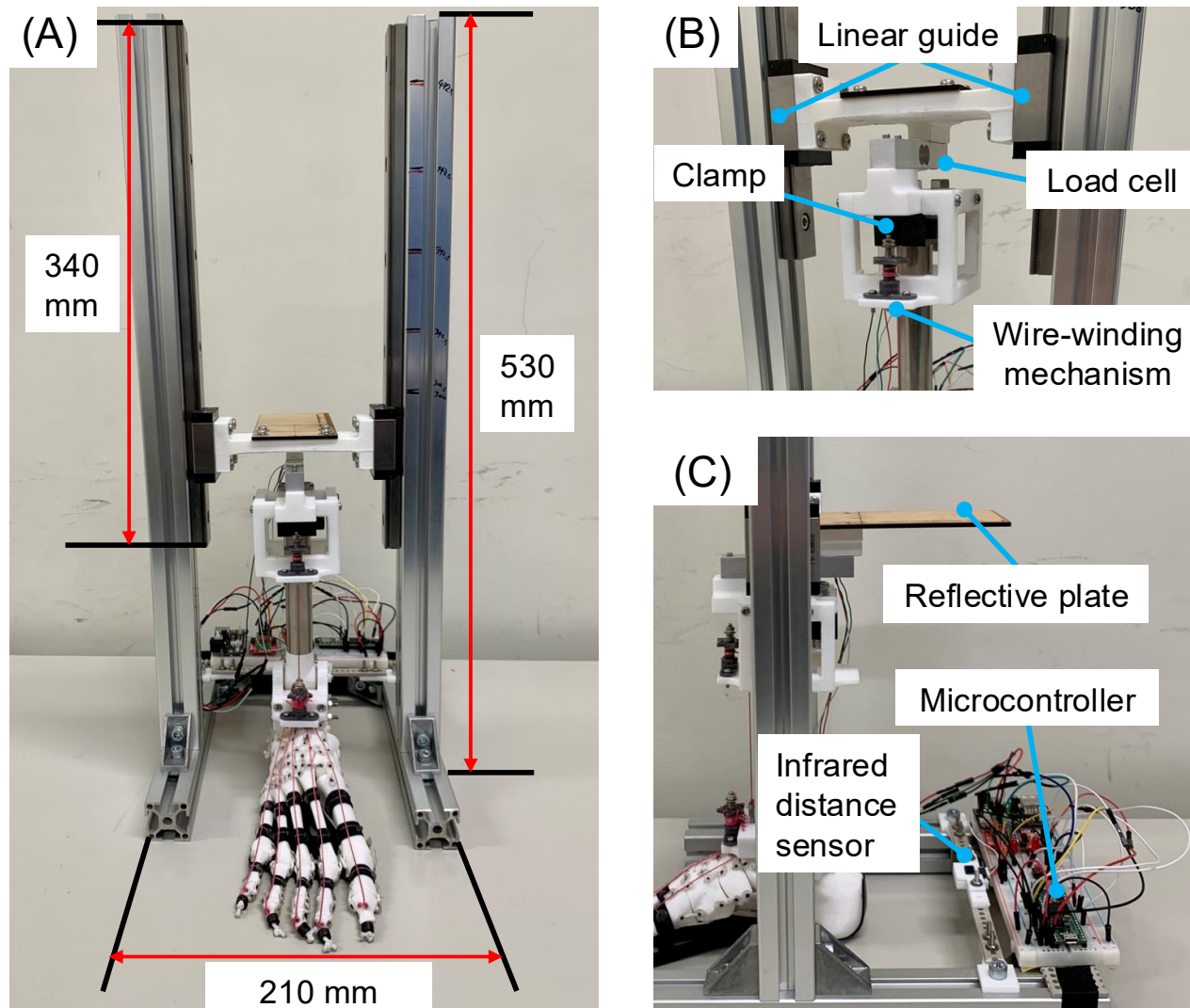


Fig. 4. Overview of the experimental apparatus. (A) Photograph and dimensions of the experimental apparatus. The apparatus is equipped with linear rails, a load cell, and infrared distance sensors, which allow the foot structures to be dropped vertically while measuring the impact force transmitted to the ankle and foot height. (B) Load cell installation position. The load

cell is placed between the two linear guides and the clamp that secures the ankle rod, enabling the forces transmitted to the ankle to be measured. (C) Infrared distance sensor placement. The infrared distance sensors are fixed at the lower part of the experimental apparatus and measure the position of a reflective plate attached for infrared detection. The two sensors are connected to a microcontroller board, and the measured data are recorded on a PC via the microcontroller.

A single-point load cell (SC133-10 kg, Sensor and Control Co., Ltd., China) was installed to measure the impact force transmitted to the ankle. As shown in Fig. 4B, the load cell was fixed between the clamp that secured the round rod and the linear guide using two mounting parts. These two mounting parts were both 3D-printed using a PLA filament. An amplifier (SparkFun Qwiic Scale-NAU7802, SparkFun Electronics, USA) was used to amplify the output voltage of the load cell and perform analog-to-digital conversion. The amplifier communicated with a microcontroller (Teensy 4.1, PJRC, USA) via I2C.

In the impact-loading experiments, an infrared distance sensor (GP2Y0E03, SHARP Corp., Japan) was used to measure the height of the foot from the ground. Fig. 4C shows the infrared distance sensor mounted on the experimental apparatus and the reflective plate used for the measurement. The sensor has a measurement range of 4–50 cm and can transmit data to a microcontroller via I2C. The sensor was fixed to the frame of the experimental apparatus and a reflective plate was attached to the falling-foot mechanism for measurement. The output values from both the load cell and infrared distance sensor were recorded on a PC via a microcontroller.

A wire traction mechanism was used to adjust the ankle angle during the foot drop. A mechanism similar to the tendon winding system of the anthropomorphic foot joint structure was installed at the top of the round rod, and dorsiflexion and plantar flexion of the ankle were achieved by fixing the end of the wire to the ankle socket (Fig. 4B). The PE braided rope, used as the tendon in the anthropomorphic foot joint structure, was also used for this purpose. Additionally, the vertically extended aluminum frame was marked at 50 mm intervals from the ground to allow for adjustment of the drop height during the experiments. The experimental apparatus had the following dimensions: height 530 mm, width 210 mm, depth 260 mm, and linear rail length 340 mm.

Experimental procedure and data analysis

The number of free-fall trials was set to 10 per condition, and the initial drop height h (the height from the ground to the sole) was varied as 50, 100, 150, and 200 mm. For each trial, the experimenter manually supported the linear guide and released it at designated height marks on the frame of the experimental apparatus, ensuring a controlled free fall from the specified positions.

The sampling rate of each sensor was set to 300 Hz, and the measurement duration was 3 s, with the foot released approximately 1 s after the start of data collection. An offset was applied to the load cell before each trial to ensure that the measured force was 0 N when the foot was unloaded or in contact with the ground. Similarly, for the infrared distance sensor, an offset was applied during post-processing such that the measured height was 0 mm when the foot was in contact with the ground.

In the experiment investigating viscoelastic changes owing to differences in skeletal structure, the experimental apparatus was equipped with the flat foot (Fig. 2C), rigid foot (Fig. 2D), and soft foot (anthropomorphic foot joint structure; Fig. 1A), each of which was

subjected to free fall. The tendons of the soft foot were removed during the experiment to eliminate the influence of factors other than the skeletal structure.

In the experiment investigating viscoelastic changes caused by differences in the ankle angle, the soft foot without tendons was subjected to free fall with the ankle angle $\theta_a = -30^\circ$, -15° , and 15° . For the $\theta_a = 0^\circ$ condition, the experimental data from the skeletal structure comparison experiment were used. The ankle angle was adjusted using the angle-indicator needle on the ankle socket and controlled via a wire-winding mechanism attached to the upper part of the ankle. To prevent the winding mechanism from loosening due to vibrations during free fall, the ankle angle was checked and readjusted before each of the 10 trials.

In the experiment investigating viscoelastic changes caused by differences in the toe angle, the flexible foot was equipped with the toe extension tendon, and the toe angle $\theta_t = 0^\circ$, 15° , 30° , and 45° for testing. The toe angle was measured using a protractor with the first metatarsal head as the center of rotation and the position of the distal phalanx of the hallux as the reference point. Similar to the ankle angle, the toe angle was checked and adjusted before each of the ten trials to ensure consistency.

The data measured by the load cell and infrared distance sensor were visualized using MATLAB (R2023a, MathWorks Inc., USA). The time-series data from each trial were aligned based on the timing of the peak impact force, and the results were averaged over 10 trials.

Simplified model analysis

Viscoelastic coefficients were identified using a spring-mass-damper model to quantitatively evaluate the viscoelasticity of the foot. In this study, the foot-landing phenomenon was modeled as an impulse response in a simple spring-mass-damper system, where the force transmitted through the spring and damper was considered equivalent to the force measured by the load cell at the ankle. The identification procedure was as follows: First, a spring-mass-damper model with unknown viscoelastic coefficients was prepared. Using the ODE solver in MATLAB Simulink, the system response was computed by applying an impulse input to the model while varying the viscoelastic coefficients. Let M denote the mass of the falling foot, x the displacement of the foot, k the elastic coefficient, c the viscous coefficient, F the impact force generated at the foot sole upon landing, and F_R the force transmitted to the ankle (Fig. S1). The equation of motion for the spring-mass-damper model is given by Eq. (1), and force F_R derived from the model is expressed by Eq. (2).

$$M\ddot{x} = -kx - c\dot{x} + F \quad (1)$$

$$F_R = kx + c\dot{x} \quad (2)$$

Here, using the drop height of the foot h , the gravitational acceleration g , and the collision duration during landing Δt , the force F can be expressed as Eq. (3).

$$F = \frac{M\sqrt{2gh}}{\Delta t} \quad (3)$$

A schematic of the model analysis and the specific parameter values used in the model analysis are provided in the Supplementary Material (Fig. S1). All parameters, except for k

and c were known and kept identical across all foot conditions. In the simulation, k was varied within the range of 10^3 to 10^7 N/m, and c was varied within 1 to 10^4 N·s/m, and the resulting response waveform of F_R was obtained. To reduce the computational load, k and c were updated using the following equations:

$$k = 10^{(3+4(n-1)/399)}; \quad (4)$$

$$c = 10^{(4(n-1)/399)}, \quad (5)$$

where n is an integer that satisfies $1 \leq n \leq 400$. The value of Δt was determined as 0.015 s, based on the duration of the main peak observed in the measured impact force waveforms. We performed a two-dimensional grid search over (k, c) on a log scale (400×400 combinations) and selected the pair that minimized the weighted waveform error.

Subsequently, the weighted error between the impact force waveforms measured in the experiments and those obtained from the numerical simulations using the model was calculated. The viscoelastic coefficients that yielded the smallest weighted error were considered as the viscoelastic coefficients of the foot used in the experiments. The weights were designed to increase the similarity between the measured and simulated waveforms, particularly focusing on the vibrations that followed the first positive peak of the impact force. Specifically, let $w(s)$ represent the weight at the s -th sampling point and s_p represent the time step at which the first positive peak appears in the measured waveform. For $1 \leq s \leq s_p$, the weight was set as $w(s) = 1.0$. For $s_p < s$, let s_{pm} denote the time step at which a positive or negative peak appears in the waveform. The weight at these points is defined as follows:

$$w(s_{pm}) = w(s_{pm} - 1) + 0.05 \sqrt{F(s_{pm})^2}, \quad (6)$$

where $F(s_{pm})$ is the impact force at step s_{pm} . For all other time steps $s \neq s_{pm}$, the weight was set to $w(s) = 1.0$. This weighting scheme ensures that the larger and more prolonged the post first peak oscillations, the greater the weights assigned to those portions, thereby allowing the identification of viscoelastic parameters that accurately reproduce the vibrational behavior following the first peak.

Viscoelastic coefficient identification was performed for data from each of the 10 trials, and the damping ratio ($c/2\sqrt{Mk}$) was calculated from the identified viscoelastic coefficients. The simulated waveforms obtained from the model analysis for each foot condition are provided in Fig. S2. Finally, the mean values of the elastic and viscous coefficients and damping ratio were calculated for each comparison.

Statistical analysis

Non-parametric statistical tests and multiple comparisons were conducted using Python to examine the significant differences between the experimental conditions in the peak impact force, identified elastic coefficient, viscous coefficient, and damping ratio. For the results related to differences in the skeletal structure, the Kruskal–Wallis test was first performed to determine whether significant differences existed between groups (significance level $\alpha =$

0.05), followed by multiple comparisons using the Steel–Dwass method ($\alpha = 0.05$). For the results related to differences in the ankle angle and toe angle, the Friedman test was first conducted to check for significant differences between groups ($\alpha = 0.05$), and then Wilcoxon signed-rank tests were performed for each pairwise comparison with the Bonferroni correction applied (adjusted significance level $\alpha = 0.008$). The statistical test results are reported in the Supplementary Material (Tables S1 and S2).

RESULTS

Viscoelastic changes due to differences in foot skeletal structure

Viscoelastic changes associated with differences in the foot skeletal structure are described below (Fig. 5). In comparing the behavior of the foot structures at the highest drop height $h = 200$ mm, where the impact force was the greatest, the flat foot and rigid-foot mechanisms rebounded from the ground upon landing, while the soft foot structure exhibited compression, with the arch flattening upon impact and subsequently returning to its original shape, achieving stability (Figs. 5A–C). The rebound height was approximately 17 mm for the flat foot and 22 mm for the rigid foot, whereas the reduction in the arch height for the soft foot was approximately 5 mm (Fig. 5D).

In examining the measured impact force waveforms, the flat foot exhibited the largest peak force, followed by vibrations lasting for approximately 70 ms after the peak (Fig. 5E). Similar post-peak vibrations were observed for the rigid foot, although its peak force was smaller and the vibration amplitude was lower than that of the flat foot. The soft foot exhibited the smallest peak force, with no vibrations reaching the negative force range, and the force gradually dissipated over approximately 35 ms. A detailed comparison of the peak impact forces showed that the flat foot had relatively higher peak forces at lower drop heights, whereas the rigid foot and soft foot had similarly smaller peak forces (Fig. 5F). At $h = 50$ mm, statistically significant differences were observed between the flat foot and rigid foot, and between the flat foot and soft foot ($p < 0.05$, Table S1), but no significant difference was found between the rigid foot and soft foot. As the drop height increased, the peak force of the rigid foot approached that of the flat foot, whereas the soft foot consistently exhibited the lowest peak force. At $h = 200$ mm, significant differences were observed between the flat foot and soft foot, and between the rigid foot and soft foot ($p < 0.05$, Table S1), but no significant difference was found between the flat foot and rigid foot.

The results of the viscoelastic coefficient identification using the simple spring-mass-damper model revealed that the elastic coefficient was significantly smaller for the soft foot (Fig. 5G), while the viscous coefficient was the smallest for the flat foot (Fig. 5H). The damping ratio, calculated from the elastic and viscous coefficients increased in the following order: flat foot, rigid foot, and soft foot (Fig. 5I). Statistically significant differences in damping ratios were observed between flat foot and rigid foot, and between the flat foot and soft foot ($p < 0.05$, Table S2).

In summary, increasing the degrees of freedom in the foot structure was associated with greater attenuation under the tested conditions.

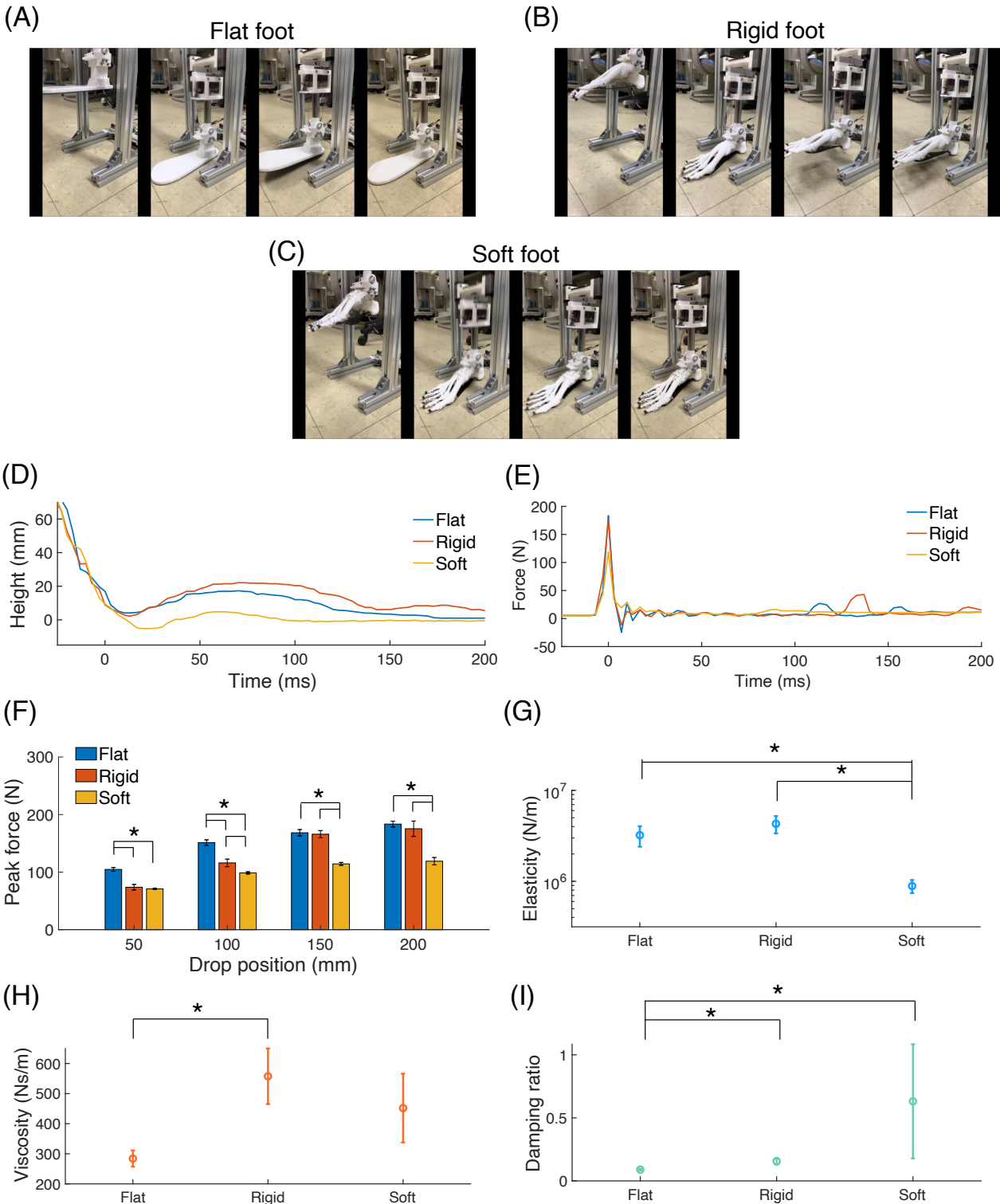


Fig. 5. Viscoelastic changes caused by differences in the skeletal structure. Snapshots of experiments for (A) flat foot, (B) rigid foot, and (C) soft foot at a drop height of $h = 200$ mm. Time-series data of (D) foot height and (E) impact force during landing. Each time-series represents the average of 10 trials, with the moment of impact set as 0 ms. (F) Peak impact forces for each drop height condition for each foot structure. (G) Elastic coefficients, (H) viscous coefficients, and (I) damping ratios estimated using the spring-mass-damper model.

Viscoelastic changes due to differences in ankle angle

The viscoelastic changes associated with variations in ankle angle θ_a are described below (Fig. 6). The results for $\theta_a = 0^\circ$ were consistent with the previously described results for the soft foot. In comparing the foot behavior immediately following landing at a drop height of $h = 200$ mm, toe-first landings at $\theta_a = -30^\circ$ and -15° resulted in the ankle rotating in the extension direction upon toe contact, followed by arch flattening when the sole made contact with the ground (Figs. 6A–C). Contrastingly, arch flattening did not occur for heel-first landing at $\theta_a = 15^\circ$, and the foot rebounded from the ground after landing (Fig. 6D). The reduction in arch height was approximately 10 mm for $\theta_a = -30^\circ$ and -15° , while the rebound height was approximately 7 mm for $\theta_a = 15^\circ$ (Fig. 6E).

In comparing the measured impact force waveforms, $\theta_a = 15^\circ$ exhibited the largest peak, accompanied by vibrations lasting approximately 80 ms (Fig. 6F). For $\theta_a = -30^\circ$ and -15° , the vibrations dissipated over approximately 40 ms. Notably, for -30° , a small initial peak was observed approximately 35 ms before the main peak, which corresponds to toe contact, and the duration of the main peak during sole contact was longer than in other conditions. In examining the peak impact forces across different drop heights, larger θ_a values (greater dorsiflexion) corresponded to higher peak forces, with the differences becoming more pronounced at higher drop heights (Fig. 6G). At $h = 50$ mm, statistically significant differences were observed between $\theta_a = -30^\circ$ and 0° , as well as $\theta_a = -15^\circ$ and 0° ($p < 0.008$, Table S1). At $h = 200$ mm, all pairwise comparisons of the four ankle angles showed significant differences ($p < 0.008$, Table S1). Notably, the peak forces for $\theta_a = -30^\circ$ remained nearly constant regardless of the drop height.

The elastic coefficients identified using the simple spring-mass-damper model were smallest for $\theta_a = -30^\circ$ and increased with larger θ_a values (Fig. 6H). The viscous coefficients were largest for $\theta_a = -15^\circ$ and tended to decrease with increasing θ_a , with $\theta_a = -30^\circ$ showing a relatively low value (Fig. 6I). Correspondingly, the damping ratios generally decreased as θ_a increased, although $\theta_a = -30^\circ$ deviated from this trend with an exceptionally low value (Fig. 6J). Significant differences in damping ratios were found between $\theta_a = -30^\circ$ and 15° , as well as between $\theta_a = -15^\circ$ and 15° ($p < 0.008$, Table S2).

In summary, toe-first landings tended to show lower peak impact forces and higher damping ratios than heel-first landings within the tested ankle-angle range.

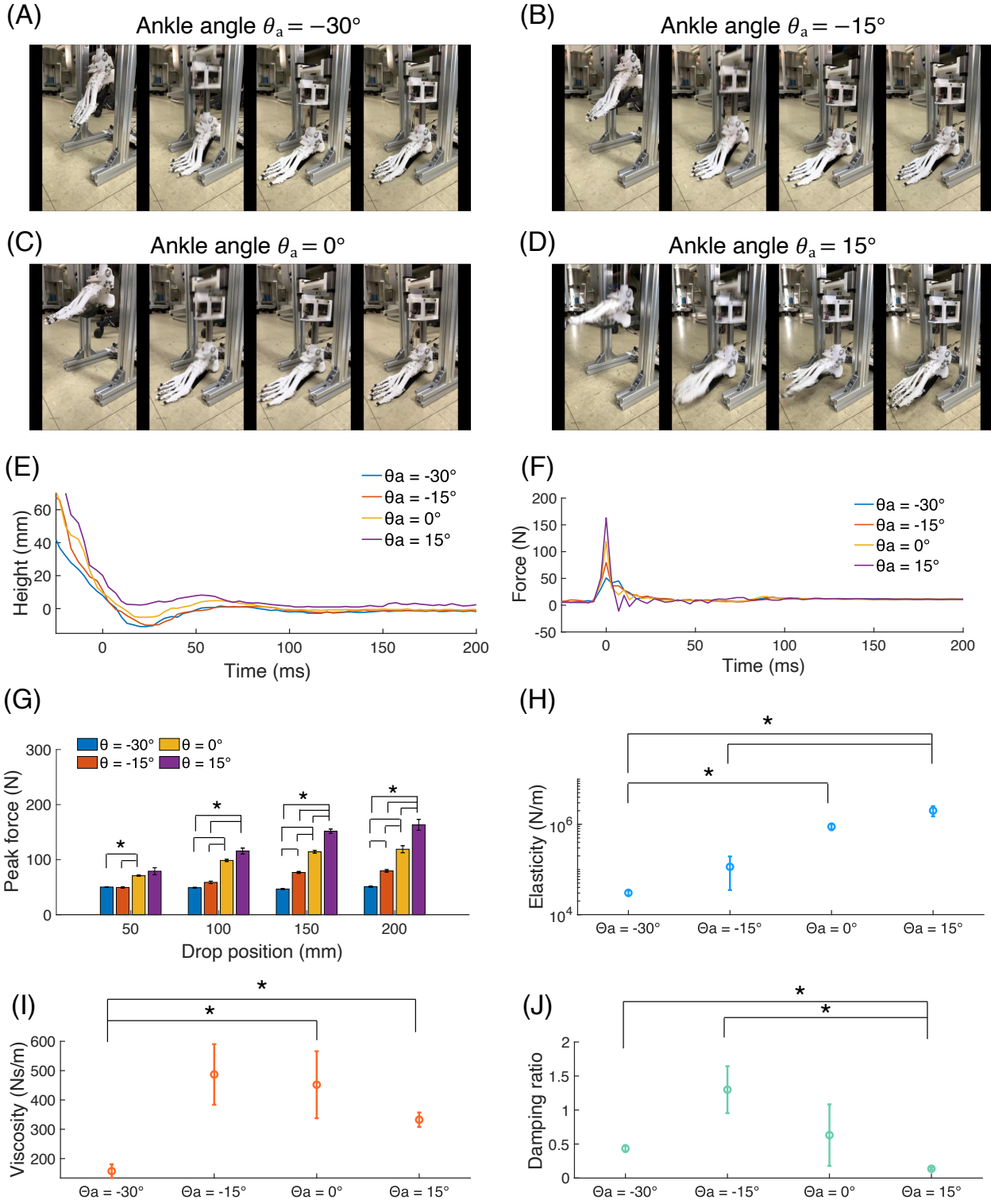


Fig. 6. Viscoelastic changes caused by differences in the ankle angle. (A) Snapshots of the experiments at a drop height of $h = 200$ mm for $\theta_a = -30^\circ$, (B) $\theta_a = -15^\circ$, (C) $\theta_a = 0^\circ$, and (D) $\theta_a = 15^\circ$. Time-series data of (E) foot height and (F) impact forces during landing. Each time-series represents the average of 10 trials, with the moment of impact set as 0 ms. (G) Graph summarizing the peak impact forces for each ankle angle across different drop height conditions. (H) Elastic coefficients, (I) viscous coefficients, and (J) damping ratios estimated using the spring-mass-damper model.

Viscoelastic changes due to differences in toe angle

The results of viscoelastic changes associated with variations in toe angle θ_t are presented below (Fig. 7). The behavior of the foot mechanism while landing at a drop height of $h = 200$ mm was consistent across all the toe angles θ_t , with arch flattening occurring upon impact, followed by recovery of the arch shape, and no rebound from the ground (Figs. 7A–D). However, a slight trend was observed where the reduction in arch height decreased as θ_t increased (i.e., as the toes extended further). At $\theta_t = 0^\circ$, the arch height reduction was approximately 8 mm, while at $\theta_t = 45^\circ$, it was approximately 2 mm (Fig. 7E).

In comparing the measured impact force waveforms, no vibrations were observed for $\theta_t = 0^\circ$ and 15° , with the peak force dissipating over approximately 33 ms. By contrast, for $\theta_t = 30^\circ$ and 45° , the peak force was slightly larger, and vibrations persisted for approximately 36 ms at $\theta_t = 30^\circ$ and 40 ms at $\theta_t = 45^\circ$ after the peak (Fig. 7F). The peak impact forces for each drop height condition showed no significant influence of θ_t at lower drop heights. However, at higher drop heights, increasing θ_t increased the peak force (Fig. 7G). At $h = 50$ mm, no significant differences were observed between any of the θ_t conditions. At $h = 200$ mm, significant differences were observed between $\theta_t = 0^\circ$ and 30° , $\theta_t = 0^\circ$ and 45° , and $\theta_t = 15^\circ$ and 45° ($p < 0.008$, Table S1).

Regarding the elastic coefficients identified using the spring-mass-damper model, the smallest value was observed at $\theta_t = 0^\circ$, and the elastic coefficients increased with θ_t (Fig. 7H). Conversely, the viscous coefficients tended to decrease as θ_t increased, with the smallest value observed at $\theta_t = 45^\circ$ (Fig. 7I). The damping ratios also tended to decrease with increasing θ_t , although the viscous coefficient for $\theta_t = 15^\circ$ was unexpectedly high, which resulted in a higher damping ratio for this condition (Fig. 7J). No significant differences were observed between any combinations of θ_t conditions in the results for viscoelastic coefficients or damping ratios.

In summary, greater toe extension tended to increase the identified elastic coefficient and decrease the damping ratio under higher drop heights, consistent with a windlass-like stiffening effect.

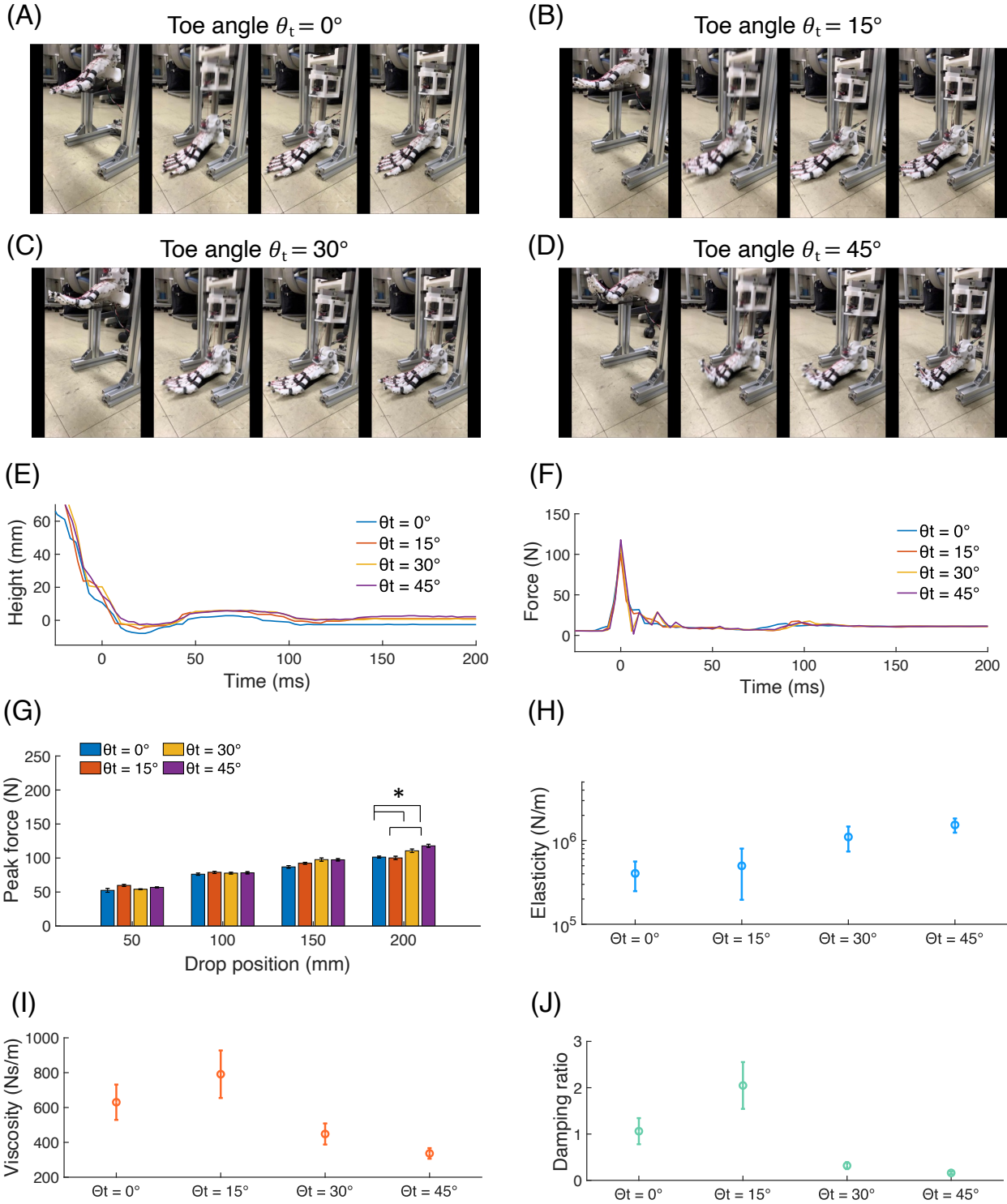


Fig. 7. Viscoelastic changes caused by differences in the toe angle. (A) Snapshots of experiments at a drop height of $h = 200$ mm for $\theta_t = 0^\circ$, (B) $\theta_t = 15^\circ$, (C) $\theta_t = 30^\circ$, and (D) $\theta_t = 45^\circ$. Time-series data of (E) foot height and (F) impact forces during landing. Each time-series represents the average of 10 trials, with the moment of impact set as 0 ms. (G) Graph summarizing the peak impact forces for each toe angle across different drop height conditions. (H) Elastic coefficients, (I) viscous coefficients, and (J) damping ratios estimated using the spring-mass-damper model.

DISCUSSION

In this study, we hypothesized that the landing posture in an anatomically grounded anthropomimetic bony and ligamentous foot architecture—designed to replicate key human skeletal geometry and ligamentous constraints rather than a generic robotic foot—can modulate the apparent viscoelastic response observed immediately after impact. To test this hypothesis using a physical testbed, we developed an anthropomimetic foot joint structure and two simplified counterparts (rigid and flat), and conducted controlled free-fall impact loading experiments. Viscoelastic coefficients were identified from the measured impact force waveform using a simplified spring-mass-damper model. The results showed systematic structure and posture-dependent changes in the identified parameters with (i) the DoF in the skeletal structure, (ii) ankle plantarflexion/dorsiflexion, and (iii) toe extension (Figs. 5–7). Collectively, these findings indicate that an anthropomimetic multi-jointed skeletal architecture can provide a tunable balance between impact attenuation and rebound in a mechanical foot, and that posture alone can modulate the apparent viscoelastic response in this structure.

The structure-dependent results (Fig. 5) suggest that introducing an arch-like, multi-jointed skeletal configuration increases the effective damping ratio during landing, compared with a flat structure. Under vertical loading, the arch deformation (Figs. 5C and 5D) is known to arise from increased joint angles in multiple small joints [36]. In our physical model, coupling forces across multiple joints likely contribute to elastic behavior, whereas friction at joint interfaces and within the arch contributes to viscous behavior. The flat and rigid feet, with physically fused joints, exhibited higher resistance to joint displacement—indicating greater apparent elasticity—than the soft foot, whose joints were constrained by ligaments; this higher elasticity promoted rebound (Figs. 5A, 5B, and 5G). In contrast, both the rigid and soft feet exhibited higher viscosity than the flat foot, which may be attributed to the dispersion of impact forces across multiple contact regions and the transmission of vibrations through multiple joints (Fig. 5H). For the soft foot in particular, sliding at joint surfaces likely converted part of the kinetic energy into heat, leading to viscosity dominating over elasticity; consequently, peak impact force decreased and the damping ratio increased (Figs. 5F and 5I). These mechanical interpretations are consistent with the notion that multi-jointed, arch-like architectures can enhance impact attenuation.

The ankle angle results (Fig. 6) demonstrate that the apparent viscoelastic response of the developed anthropomimetic foot joint structure can be tuned by landing posture at the ankle. In our experiments, heel-first landings exhibited higher apparent elasticity (Fig. 6H), whereas toe-first landings exhibited higher apparent viscosity (Fig. 6I). In the mechanical structure, a heel-first posture likely transmits impact forces to the ankle through fewer joints, thereby reducing frictional dissipation and increasing rebound. Conversely, a toe-first posture transmits forces through multiple joints, increasing frictional effects at more joint interfaces and increasing energy dissipation, resulting in a higher damping ratio (Fig. 6J). Qualitatively, these posture-dependent trends are consistent with reported differences in human landing strategies (e.g., heel-first contacts in economical walking versus softer toe-involved contacts in certain landing tasks) [37–39]. In the present physical testbed, active neuromuscular control and proximal joints are not represented; therefore, the comparison to human strategies is qualitative. Notably, the simulation results for $\theta_a = -30^\circ$ indicated an anomalously low viscous coefficient (Fig. 6I), suggesting that the simple spring-mass-damper model can incur substantial modeling errors under certain conditions (Fig. S2F). This motivates future work with more detailed models.

The toe angle results (Fig. 7) indicate that toe extension can alter the apparent viscoelastic parameters under higher landing loads in the developed structure, in line with biomechanical accounts of the windlass mechanism [5,9]. In our structure, increasing toe angle under high-load conditions reduced the damping ratio (Figs. 7G and 7J). A plausible mechanical explanation is that increased tension in the plantar-fascia-like element raises contact pressure across small joints, increasing coupling forces (enhancing elasticity) while reducing sliding at joint interfaces (reducing viscous resistance) (Figs. 7H and 7I). These trends are consistent with prior analyses of foot viscoelastic models [17,18]. We interpret these results as evidence that toe posture, through a windlass-like stiffening effect, can shift the trade-off between rebound and dissipation in an anthropomimetic foot joint structure; however, quantitative equivalence to human *in vivo* behavior remains to be established.

The present study intentionally focused on skeletal structure and passive posture within an anthropomimetic foot joint structure to isolate their contributions to landing viscoelasticity. Consequently, we did not model or incorporate the knee and hip joints, active muscle-tendon actuation, or subject-specific soft tissue material properties. Moreover, the material fidelity of the ligaments, plantar-fascia-like element, and other compliant tissues can be improved. Future work should extend the developed structure toward greater anatomical and material accuracy and integrate it into a legged robotic platform with knee and hip joints. Such a platform would enable evaluation of ground reaction forces and kinematics under more dynamic locomotion tasks and provide a stronger basis for comparing mechanical trends with human experimental observations. Beyond robotics, the demonstrated posture- and morphology-dependent modulation of landing viscoelasticity suggests potential applications in sports injury prevention, rehabilitation interventions, and footwear design, where impact attenuation and rebound characteristics are critical.

CONCLUSION

In this study, we developed an anatomically grounded anthropomimetic foot joint structure aimed at replicating key human skeletal geometry and ligamentous constraints, and used it as a physical testbed to examine how morphology and posture shape the immediate post-landing viscoelastic response. Using controlled free-fall impact loading experiments and spring-mass-damper identification from impact-force waveforms, we demonstrated systematic structure- and posture-dependent modulation of apparent viscoelastic parameters. Compared with a flat foot and a rigid foot, the multi-jointed anthropomimetic structure exhibited greater impact-force attenuation and a higher damping ratio during landing, indicating that increased skeletal degrees of freedom can enhance energy dissipation in this mechanically realistic architecture. Ankle posture strongly tuned the landing response, with toe-first landings tending to reduce peak impact forces and increase damping relative to heel-first landings, and toe extension under higher drop heights tending to increase the effective elastic coefficient and reduce the damping ratio, consistent with a windlass-like stiffening effect in the developed structure. Collectively, these results show that morphology and passive posture alone can tune the trade-off between impact attenuation and rebound in an anthropomimetic mechanical foot, with implications for the design of robotic feet, sports injury prevention, rehabilitation interventions, and footwear. Future work will focus on improving anatomical and material fidelity and integrating the developed structure into a legged robotic platform with knee and hip joints.

ACKNOWLEDGMENTS

Author contributions: Conceived and designed the experiments: SH, ST. Performed the experiments: SH. Analyzed the data: SH, ST. Discussed the results and wrote the paper: SH, YJ, HY, ST. All authors gave final approval for publication.

Funding: This work was supported by the Japan Society for the Promotion of Science (JSPS) KAKENHI under Grant JP22K04025 and Grant JP23H00166, and in part by JKA through Promotion Funds from KEIRIN RACE.

Competing interests: The authors declare that this research was conducted in the absence of any commercial, financial, or non-financial interests.

DATA AVAILABILITY

All data and materials supporting this study, including the measured raw data, 3D CAD files, 3D-printable part files, and a supplementary video, are publicly available in the GitHub repository to facilitate reproducibility (<https://github.com/TogoLab/anthropomorphic-foot-joint-structure>).

SUPPLEMENTARY MATERIALS

Supplementary materials (Video S1 and Data S1) are available in the GitHub repository (<https://github.com/Togolab/anthropomorphic-foot-joint-structure>).

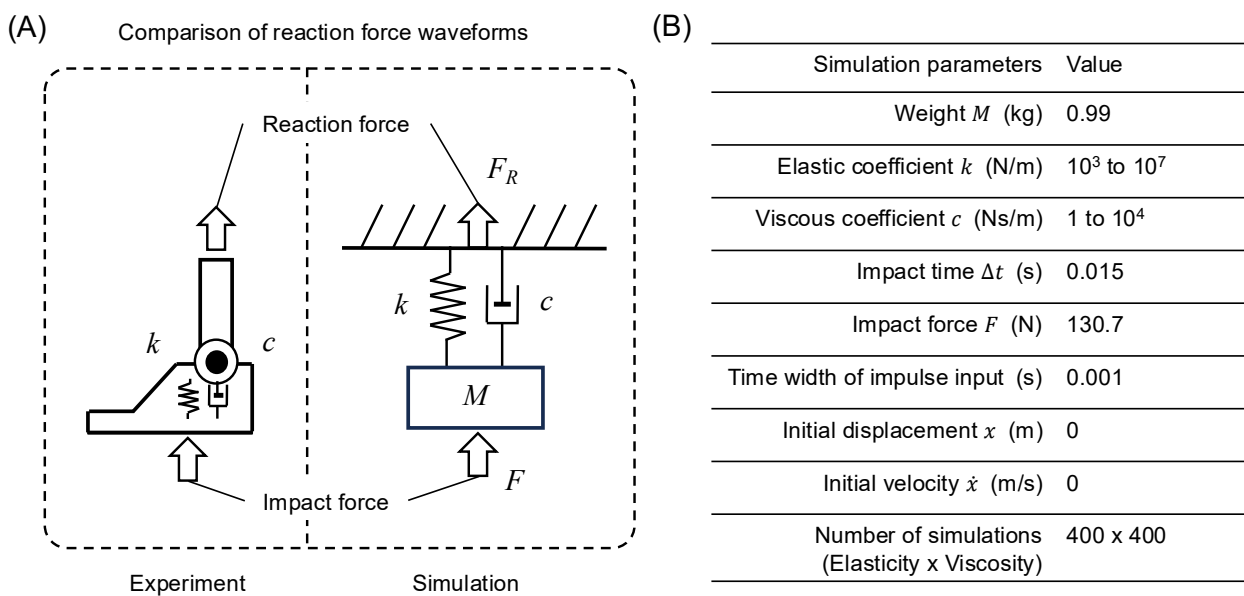


Fig. S1. Schematic diagram of the model analysis and parameter values. (A) Spring-mass-damper model of the foot. In this study, each foot structure is modeled as a spring-mass-damper system with unknown viscoelastic coefficients. The viscoelastic coefficients are determined by comparing the impact force waveforms transmitted to the ankle, measured in the experiment, with the model response obtained through the model analysis. (B) Parameter values used in the model analysis. Each parameter is determined based on the weight of the fabricated foot mechanism, drop height in the experiment, and measured impact force waveforms.

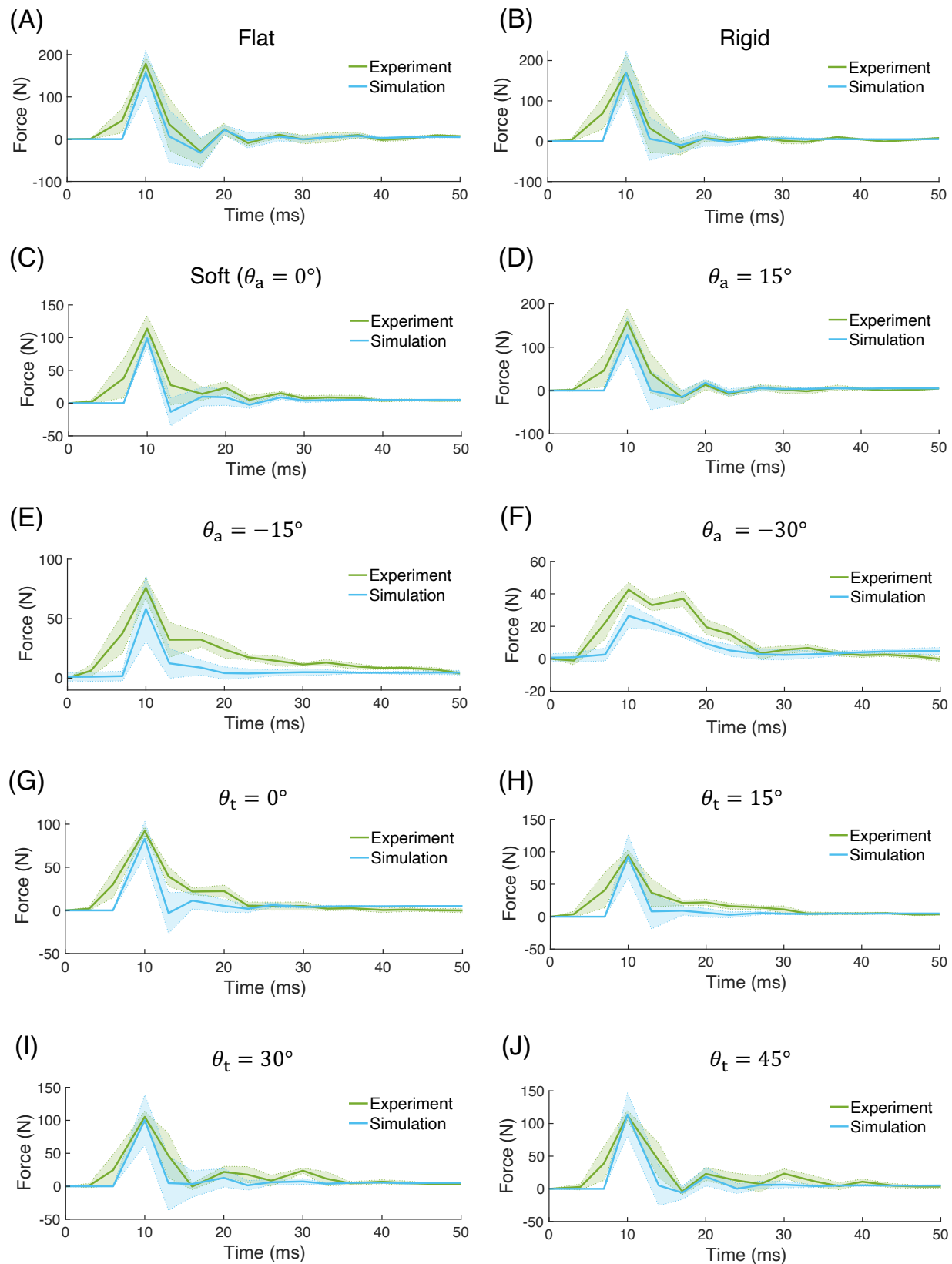


Fig. S2. Comparison of measured and simulated impact force waveforms. (A–C) Differences in waveforms based on the skeletal structure. (C–F) Differences in waveforms based on the ankle angle. (G–J) Differences in waveforms based on the toe angle. The impact force waveforms of each foot mechanism at a drop height of $h = 200$ mm are compared with the simulated waveforms obtained from the model analysis, where the viscoelastic coefficients were identified.

Table S1. *p*-values and significance levels for the statistical tests on peak impact force. The asterisk (*) indicates a statistically significant difference. For simplification, the names of the statistical tests are abbreviated as follows; K.W. : Kruskal–Wallis Test ($\alpha = 0.05$), S.D. : Steel–Dwass Test ($\alpha = 0.05$), Fri. : Friedman Test ($\alpha = 0.05$) and W.S.R. : Wilcoxon Signed-Rank Test ($\alpha = 0.008$). The significance level for each test is indicated by α .

Comparative condition	Drop height <i>h</i> (mm)	Test type	<i>p</i> -value		
Skeleton	50	K.W.	< 0.0010*		
		S.D.	Flat vs. Rigid	Flat vs. Soft	Rigid vs. Soft
			< 0.0010*	< 0.0010*	0.17
		K.W.	< 0.0010*		
	100	S.D.	Flat vs. Rigid	Flat vs. Soft	Rigid vs. Soft
			0.0025*	< 0.0010*	0.011*
		K.W.	< 0.0010*		
		S.D.	Flat vs. Rigid	Flat vs. Soft	Rigid vs. Soft
			0.90	< 0.0010*	0.0015*
	150	K.W.	< 0.0010*		
		S.D.	Flat vs. Rigid	Flat vs. Soft	Rigid vs. Soft
			0.71	< 0.0010*	0.022*
		Fri.	0.0014*		
Ankle	50	W.S.R.	$\theta_a = -30^\circ$ vs. -15°	$\theta_a = -30^\circ$ vs. 0°	$\theta_a = -30^\circ$ vs. -15°
			0.85	0.0020*	0.0098
			$\theta_a = -15^\circ$ vs. 0°	$\theta_a = -15^\circ$ vs. 15°	$\theta_a = 0^\circ$ vs. 15°
			0.0020*	0.0098	0.32
	100	Fri.	< 0.0010*		
		W.S.R.	$\theta_a = -30^\circ$ vs. -15°	$\theta_a = -30^\circ$ vs. 0°	$\theta_a = -30^\circ$ vs. 15°
			0.014	0.0020*	0.0020*
			$\theta_a = -15^\circ$ vs. 0°	$\theta_a = -15^\circ$ vs. 15°	$\theta_a = 0^\circ$ vs. 15°
		W.S.R.	0.0020*	0.0020*	0.037
	150	Fri.	< 0.0010*		
		W.S.R.	$\theta_a = -30^\circ$ vs. -15°	$\theta_a = -30^\circ$ vs. 0°	$\theta_a = -30^\circ$ vs. 15°
			0.0020*	0.0020*	0.0020*
			$\theta_a = -15^\circ$ vs. 0°	$\theta_a = -15^\circ$ vs. 15°	$\theta_a = 0^\circ$ vs. 15°
		W.S.R.	0.0020*	0.0020*	0.0020*
	200	Fri.	< 0.0010*		
		W.S.R.	$\theta_a = -30^\circ$ vs. -15°	$\theta_a = -30^\circ$ vs. 0°	$\theta_a = -30^\circ$ vs. 15°
			0.0020*	0.0020*	0.0020*

		$\theta_a = -15^\circ$ vs. 0°	$\theta_a = -15^\circ$ vs. 15°	$\theta_a = 0^\circ$ vs. 15°
		0.0020*	0.0020*	0.0020*
		Fri.	0.17	
		$\theta_t = 0^\circ$ vs. 15°	$\theta_t = 0^\circ$ vs. 30°	$\theta_t = 0^\circ$ vs. 45°
50	W.S.R.	0.084	0.85	0.32
		$\theta_t = 15^\circ$ vs. 30°	$\theta_t = 15^\circ$ vs. 45°	$\theta_t = 30^\circ$ vs. 45°
		0.014	0.11	0.020
		Fri.	0.95	
		$\theta_t = 0^\circ$ vs. 15°	$\theta_t = 0^\circ$ vs. 30°	$\theta_t = 0^\circ$ vs. 45°
100	W.S.R.	0.43	0.56	0.43
		$\theta_t = 15^\circ$ vs. 30°	$\theta_t = 15^\circ$ vs. 45°	$\theta_t = 30^\circ$ vs. 45°
Toe		0.77	0.70	0.85
		Fri.	0.0087*	
		$\theta_t = 0^\circ$ vs. 15°	$\theta_t = 0^\circ$ vs. 30°	$\theta_t = 0^\circ$ vs. 45°
150	W.S.R.	0.13	0.014	0.0098
		$\theta_t = 15^\circ$ vs. 30°	$\theta_t = 15^\circ$ vs. 45°	$\theta_t = 30^\circ$ vs. 45°
		0.11	0.020	1.0
		Fri.	< 0.0010*	
		$\theta_t = 0^\circ$ vs. 15°	$\theta_t = 0^\circ$ vs. 30°	$\theta_t = 0^\circ$ vs. 45°
200	W.S.R.	0.77	0.0020*	0.0039*
		$\theta_t = 15^\circ$ vs. 30°	$\theta_t = 15^\circ$ vs. 45°	$\theta_t = 30^\circ$ vs. 45°
		0.0098	0.0039*	0.064

Table S2. *p*-values and significance levels for the statistical tests on elastic coefficients, viscous coefficients, and damping ratios. The asterisk (*) indicates a statistically significant difference. For simplification, the names of the statistical tests are abbreviated as follows: K.W. : Kruskal–Wallis Test ($\alpha = 0.05$), S.D. : Steel–Dwass Test ($\alpha = 0.05$), Fri. : Friedman Test ($\alpha = 0.05$) and W.S.R. : Wilcoxon Signed-Rank Test ($\alpha = 0.008$). The significance level for each test is indicated by α .

Comparative condition	Viscoelastic Properties	Test type	<i>p</i> -value		
	Elastic coefficient	K.W.	< 0.0010*		
		S.D.	Flat vs. Rigid	Flat vs. Soft	Rigid vs. Soft
			0.54	0.0047*	0.0025*
Skeleton	Viscous coefficient	K.W.	0.014*		
		S.D.	Flat vs. Rigid	Flat vs. Soft	Rigid vs. Soft
			0.010*	0.40	0.27
	Damping ratio	K.W.	< 0.0010*		
		S.D.	Flat vs. Rigid	Flat vs. Soft	Rigid vs. Soft

		0.020	< 0.0010*	0.17
		Fri.	< 0.0010*	
Ankle	Elastic coefficient	$\theta_a = -30^\circ$ vs. -15°	$\theta_a = -30^\circ$ vs. 0°	$\theta_a = -30^\circ$ vs. -15°
		0.43	0.0039*	0.0020*
		$\theta_a = -15^\circ$ vs. 0°	$\theta_a = -15^\circ$ vs. 15°	$\theta_a = 0^\circ$ vs. 15°
	Viscous coefficient	0.0098	0.0039*	0.080
		Fri.	0.0031*	
		$\theta_a = -30^\circ$ vs. -15°	$\theta_a = -30^\circ$ vs. 0°	$\theta_a = -30^\circ$ vs. 15°
Toe	Damping ratio	0.020	0.0020*	0.0020*
		$\theta_a = -15^\circ$ vs. 0°	$\theta_a = -15^\circ$ vs. 15°	$\theta_a = 0^\circ$ vs. 15°
		0.91	0.13	0.70
	Elastic coefficient	Fri.	0.0029*	
		$\theta_a = -30^\circ$ vs. -15°	$\theta_a = -30^\circ$ vs. 0°	$\theta_a = -30^\circ$ vs. 15°
		0.064	0.11	0.0039*
Toe	Viscous coefficient	$\theta_a = -15^\circ$ vs. 0°	$\theta_a = -15^\circ$ vs. 15°	$\theta_a = 0^\circ$ vs. 15°
		0.16	0.0059*	0.049
		Fri.	0.069	
	Elastic coefficient	$\theta_t = 0^\circ$ vs. 15°	$\theta_t = 0^\circ$ vs. 30°	$\theta_t = 0^\circ$ vs. 45°
		0.43	0.28	0.0059
		$\theta_t = 15^\circ$ vs. 30°	$\theta_t = 15^\circ$ vs. 45°	$\theta_t = 30^\circ$ vs. 45°
	Viscous coefficient	0.28	0.13	0.56
		Fri.	0.086	
		$\theta_t = 0^\circ$ vs. 15°	$\theta_t = 0^\circ$ vs. 30°	$\theta_t = 0^\circ$ vs. 45°
Toe	Damping ratio	0.38	0.23	0.037
		$\theta_t = 15^\circ$ vs. 30°	$\theta_t = 15^\circ$ vs. 45°	$\theta_t = 30^\circ$ vs. 45°
		0.11	0.020	0.13
	Elastic coefficient	Fri.	0.019*	
		$\theta_t = 0^\circ$ vs. 15°	$\theta_t = 0^\circ$ vs. 30°	$\theta_t = 0^\circ$ vs. 45°
		0.16	0.11	0.014
Toe	Viscous coefficient	$\theta_t = 15^\circ$ vs. 30°	$\theta_t = 15^\circ$ vs. 45°	$\theta_t = 30^\circ$ vs. 45°
		0.037	0.014	0.027
		Fri.	0.019*	

Video S1. Representative footage of the impact loading experiments (available in the GitHub repository under media/).

Data S1. Raw time-series data of the impact force transmitted to the ankle and the drop height measured during the impact loading experiments (available in the GitHub repository under raw_data/).

REFERENCES

[1] Susman R. Evolution of the human foot: evidence from plio-pleistocene hominids. *Foot Ankle Int.* 1983; 3:365-376. <https://doi.org/10.1177/107110078300300605>

[2] Harcourt-Smith WEH, Aiello LC. Fossils, feet and the evolution of human bipedal locomotion. *J Anat.* 2004; 204:403-416. <https://doi.org/10.1111/j.0021-8782.2004.00296.x>

[3] McNutt E, Zipfel B, DeSilva J. The evolution of the human foot. *Evol Anthropol.* 2018;27, 197-217. <https://doi.org/10.1002/evan.21713>

[4] Holowka N, Lieberman D. Rethinking the evolution of the human foot: insights from experimental research. *Exp Biol.* 2018;221, jeb174425. <https://doi.org/10.1242/jeb.174425>

[5] Hicks JH. The mechanics of the foot. II. The plantar aponeurosis and the arch. *J Anat.* 1954;88, 25-30. PMID: <https://pubmed.ncbi.nlm.nih.gov/13129168/>

[6] Ker R, Bennett M, Bibby S, Kester R, Alexander R. The spring in the arch of the human foot. *Nature.* 1987;325, 147-149. <https://doi.org/10.1038/325147a0>

[7] Ren L, Howard D, Ren L, Nester C, Tian L. A phase-dependent hypothesis for locomotor functions of human foot complex. *J Bionic Eng.* 2008;5, 175-180. [https://doi.org/10.1016/S1672-6529\(08\)60022-0](https://doi.org/10.1016/S1672-6529(08)60022-0)

[8] Venkadesan M, Yawar A, Eng CM, Dias MA, Singh DK, Tommasini SM, Haims AH, Bandi MM, Mandre S. Stiffness of the human foot and evolution of the transverse arch. *Nature.* 2020;579, 97-100. <https://doi.org/10.1038/s41586-020-2053-y>

[9] Welte L, Kelly LA, Kessler SE, Lieberman DE, D'Andrea SE, Lichtwark GA, Rainbow MJ. The extensibility of the plantar fascia influences the windlass mechanism during human running. *Proc R Soc B.* 2021:288, 20202095, <https://royalsocietypublishing.org/doi/10.1098/rspb.2020.2095>

[10] Hildebrand M. How animals run. *Sci Am.* 1960; 202, 148-160. <https://www.jstor.org/stable/24940484>

[11] Polly P, Hall B. Limbs in mammalian evolution. *Fins into Limbs: Evolution, Development, and Transformation.* 2006:245–268. <https://doi.org/10.7208/9780226313405>

[12] Cunningham C, Schilling N, Anders C, Carrier D. The influence of foot posture on the cost of transport in humans. *J Exp Biol.* 2010;213, 790-797. <https://doi.org/10.1242/jeb.038984>

[13] Dick T, Clemente C. Where have all the giants gone? How animals deal with the problem of size. *Plos Biol.* 2017;15, e2000473. <https://doi.org/10.1371/journal.pbio.2000473>

[14] Gilchrist L, Winter D. A two-part, viscoelastic foot model for use in gait simulations. *J Biomech.* 1996;29, 795-798. [https://doi.org/10.1016/0021-9290\(95\)00141-7](https://doi.org/10.1016/0021-9290(95)00141-7)

[15] Güler H, Berme N, Simon S. A viscoelastic sphere model for the representation of plantar soft tissue during simulations. *J Biomech.* 1998;31, 847-853. [https://doi.org/10.1016/S0021-9290\(98\)00085-2](https://doi.org/10.1016/S0021-9290(98)00085-2)

[16] Shourijeh S, McPhee J. Foot-ground contact modeling within human gait simulations: from Kelvin–Voigt to hyper-volumetric models. *Multibody Syst Dyn.* 2015;35, 393-407. <https://doi.org/10.1007/s11044-015-9467-6>

[17] Takashima T, Fujimoto H, Takanishi A. Analysis of the human foot arch viscoelasticity using the simple model of the arch support elements. *Trans Jpn Soc Mech Eng C*. 2003;69, 2397-2402. <https://doi.org/10.1299/kikaic.69.2397> (in Japanese)

[18] Hashimoto K, Takezaki Y, Hattori K, Kondo H, Takashima T, Lim H, Takanishi A. A study of function of foot's medial longitudinal arch using biped humanoid robot. *In Proc IEEE/RSJ IROS2010*. 2010;2206-2211. <https://doi.org/10.1109/IROS.2010.5650414>

[19] Wright D, Rennels DA. Study of the elastic properties of plantar fascia. *J Bone Joint Surg Am*. 1964;46, 482-492. <https://doi.org/10.2106/00004623-196446030-00002>

[20] Carlson R, Fleming L, Hutton W. The biomechanical relationship between the tendoachilles, plantar fascia and metatarsophalangeal joint dorsiflexion angle. *Foot Ankle Int*. 2000;21, 18-25. <https://doi.org/10.1177/107110070002100104>

[21] Sakagami Y, Watanabe R, Aoyama C, Matsunaga S, Higaki N, Fujimura K. The intelligent ASIMO: System overview and integration. *In Proc IEEE/RSJ IROS2002*, 2478-2483. <http://dx.doi.org/10.1109/IRDS.2002.1041641>

[22] Guizzo E. By leaps and bounds: An exclusive look at how Boston dynamics is redefining robot agility. *IEEE Spectrum*. 2019;56, 34-39. <https://doi.org/10.1109/MSPEC.2019.8913831>

[23] Hashimoto K, Takezaki Y, Hattori K, Kondo H, Takashima T, Lim H. A study of function of foot's medial longitudinal arch using biped humanoid robot. *In Proc IEEE/RSJ IROS2010*. 2206-2211. <https://doi.org/10.1109/IROS.2010.5650414>.

[24] Narioka K, Homma T, Hosoda K. Humanlike ankle-foot complex for a biped robot. *In Proc Humanoids2012*. 15-20. <https://doi.org/10.1109/HUMANOIDS.2012.6651493>

[25] Davis S, Caldwell D. The design of an anthropomorphic dexterous humanoid foot. *In Proc IEEE/RSJ IROS2010*. 2200-2205. <https://doi.org/10.1109/IROS.2010.5649756>

[26] Piazza C, Della C, Gian S, Gasparri M, Catalano MG, Grioli G, Garabini M. Toward an adaptive foot for natural walking. *In Proc Humanoids2016*. 1204-1210. <https://doi.org/10.1109/HUMANOIDS.2016.7803423>

[27] Xu Z, Todorov E. Design of a highly biomimetic anthropomorphic robotic hand towards artificial limb regeneration. *In Proc IEEE/RSJ ICRA2016*. 3485-3492. <https://doi.org/10.1109/ICRA.2016.7487528>

[28] Hughes JAE, Maiolino P, Iida F. An anthropomorphic soft skeleton hand exploiting conditional models for piano playing. *Science Robotics*. 2018;3, eaau3098. <https://doi.org/10.1126/scirobotics.aau3098>

[29] Zhu Y, Wei G, Ren L, Luo Z, Shang J. An anthropomorphic robotic finger with innate human-finger-like biomechanical advantages part I: Design, ligamentous joint, and extensor mechanism. *IEEE Trans Robot*. 2023;39, 485-504. <https://doi.org/10.1109/TRO.2022.3200006>

[30] Zhu Y, Wei G, Ren L, Luo Z, Shang J. An anthropomorphic robotic finger with innate human-finger-like biomechanical advantages part II: Flexible tendon sheath and grasping demonstration. *IEEE Trans Robot*. 2023;39, 505-520. <https://doi.org/10.1109/TRO.2022.3200143>

[31] Obata Y, Jiang Y, Yokoi H, Togo S. Design of anthropomorphic robotic wrist joint and forearm. *in Proc IEEE SMC2023*. 1766-1771, <https://doi.org/10.1109/SMC53992.2023.10394226>

[32] Yang H, Wei G, Ren, L. Development and characteristics of a highly biomimetic robotic shoulder inspired by musculoskeletal mechanical intelligence. *IEEE Trans Robot.* 2024;40, 2672-2691. <https://doi.org/10.1109/TRO.2024.3390057>

[33] Yang H, Wei G, Ren L. Enhancing the performance of a biomimetic robotic elbow-and-forearm system through bionics-inspired optimization. *IEEE Trans Robot.* 2024;40, 2692-2711. <https://doi.org/10.1109/TRO.2024.3386615>

[34] Schünke M, Schulte E, Schumacher U. PROMETHEUS Allgemeine Anatomie und Bewegungssystem LernAtlas der Anatomie, Third Japanese edition (tr. Sakai, T. & Matumura, J.) 458-479 (Igaku-Shoin Ltd., Tokyo, 2017)

[35] Database Center for Life Science, BodyParts3D, <https://lifesciencedb.jp/bp3d/> (Accessed 2023).

[36] Kitaoka H, Lundberg A, Luo Z, An K. Kinematics of the normal arch of the foot and ankle under physiologic loading. *Foot Ankle Int.* 1995;16, 492-499. <https://doi.org/10.1177/107110079501600806>

[37] Bramble D, Lieberman D. Endurance running and the evolution of Homo. *Nature.* 2004;432, 345-352. <https://doi.org/10.1038/nature03052>

[38] McKinley P, Pedotti A. Motor strategies in landing from a jump: the role of skill in task execution. *Exp Brain Res.* 1992;90, 427-440. <https://doi.org/10.1007/BF00227257>

[39] Zhang S, Bates B, Dufek J. Contributions of lower extremity joints to energy dissipation during landings. *Med Sci Sports Exerc.* 2000;32, 812-819. <https://doi.org/10.1097/00005768-200004000-00014>